Calibration of a 2D Laser Scanner System and Rotating Platform using a Point-Plane Constraint

Laksono Kurnianggoro, Van-Dung Hoang, and Kang-Hyun Jo*

Graduate School of Electrical Engineering
University of Ulsan, Korea
{laksono, hvdung}@islab.ulsan.ac.kr, acejo@ulsan.ac.kr
*Corresponding Author

Abstract. The purpose of this study was to produce a low cost 3D scanner system using a rotating 2D laser scanner. There are two key parameters of this system, the rotation axis and the rotation radius. These two parameters were extracted through a calibration procedure. The calibration requires a planar checkerboard calibration pattern. Several poses were scanned to obtain the observation data. The rotation axis and the rotation radius were extracted by solving a linear equation constructed from a point-plane constraint, where all points lie on a plane and have a zero dot product to the surface normal to the plane. This method was tested on a simulation environment by generating synthetic data of the scanned calibration pattern. A comprehensive analysis was carried out to evaluate the performance of the proposed method. From the simulation results, it was demonstrated that this method achieved highly accurate results with an orientation error of 0.018 degree and a radius error of 0.2 cm.

Keywords: calibration, laser range finder, 3D scanner.

1.   Introduction

In the past few years, intelligent systems has been intensively studied [9, 1, 18, 12]. One of the research field is involving 3D sensing systems, including 3D reconstruction [5], localization [7], path planning [8], segmentation [17, 23], and recognition [21]. 3D data provides more information than a 2D image, allowing better performance of the method. Previous research [21] shows that object recognition using 3D data and a SVM classifier [2, 3] provides better results than using only 2D data.

There are currently several types of 3D sensors available including a stereo camera, time-of-flight camera, structured light camera (Kinect), and 3D laser scanner. Among them, a 3D laser scanner provides the best measurement results. It is able to provide a long-range measurement with relatively low noise. However, despite its excellent performance, the measurement system such as Velodyne HDL-64 is quite expensive compared to other 3D sensors.

A laser range finder (LRF) is a 2D laser scanner system. Its measurement capability is confined to a single scanning plane. However, it is able to provide high precision measurement results for indoor and outdoor applications. A typical outdoor LRF system such as SICK LMS 511 is able to measure an object at 80 m with a statistical error varying from 6 mm to 50 mm, depending on the measured distance and the reflection rate.

Basically, the 2D laser sensor achieves similar measurement performance as a 3D laser scanner. However, the 2D sensor is cheaper than 3D laser measurement systems.

By rotating a 2D laser scanner, a low cost 3D sensing system can be developed. A laser range finder system, such as the SICK LMS series and Hokuyo Lidar series, is able to measure one scanning line from the scene. By combining the scanning results from all rotation angles, the scanning results from the whole scene are obtained.

A rotating 2D laser scanner system is modeled as an object which revolves around an axis. In this system, two parameters are extracted, the rotation axis and the rotation radius. Generally, the rotation axis does not coincide with any axis of the LRF coordinate frame. A calibration method is performed to extract the rotation axis and the rotation radius.

This paper proposes a novel calibration method which is able to extract the rotation axis and rotation radius from a rotating 2D laser scanner system[1]. In this method, a planar calibration pattern was used. The calibration pattern was scanned using several different poses. For each pose, measurement data (points) from a specific rotation angle were obtained. These measured points are represented as virtual points. By rotating the virtual points with their corresponding rotation angle, their original positions, which are the scanned positions, are recovered. A linear equation was constructed based on the relationship among the virtual point, original point, rotation axis, rotation radius, and parameter of the calibration plane. Using the data obtained from several poses of the calibration pattern, the initial estimation of the rotation axis and rotation radius can be extracted by solving the linear equations.

This paper is organized as follows. In the next section, a brief review of the previously available calibration methods is presented. In sections 3 and 4, a comprehensive explanation of the proposed method is covered. Section 3 focuses on the geometrical model while section 4 focuses on the calibration procedure. In section 5, several simulation schemes and their results are presented. Finally, a brief conclusion is presented.

2.   Related Works

Calibration methods for a rotating 2D laser system have been studied intensively over the past few years. These proposed methods can be distinguished based on their rotating system geometrical model or calibration pattern.

A calibration method was presented in [10] proposed to use a calibration pattern with the special shape of a stereoscopic checkerboard. This is a 3D pattern with several black cubes placed in a checkerboard formation, forming a checkerboard with extruded black squares. In this method, a rotating LRF and a camera are used. The two sensors are used to scan the calibration pattern. Hence, 3D range data and an intensity image are obtained. In the calibration process, the corresponding corner features from the intensity image and 3D range data are extracted. By analyzing the relationship between these corresponding features, the calibration parameters are extracted.

In addition, another special calibration pattern with a planar arrow shape has been proposed [4]. The author mentioned that by using this right angle outline calibration board, better calibration precision can be obtained. In this algorithm, several important properties

---

[1] This paper is significantly extended from the paper [11] in International Conference on Computational Collective Intelligence Technologies and Applications, 2014.

Fig. 1. A LRF sensor is mounted on a rotation base to construct the 3D laser scanner system.

are considered including the linearity, perpendicular, and co-planarity properties. Using these observable properties, the calibration parameters are calculated.

A pyramid-like calibration pattern has previously been used [26]. The calibration pattern consists of a pyramid with holes where the bold lines indicate virtual polypod legs formed by the intersection of pyramid faces. With this kind of shape, the calibration pattern is reliable and stable for detection.

A calibration method using a conventional checkerboard pattern has been evaluated [19]. This method used a camera as a reference point to determine the relative pose of the 2D laser sensor at two different rotation angles. At each rotation angle, the LRF poses are approximated by performing a camera-LRF calibration procedure. A total of two LRF poses should be extracted. Based on two poses of the rotated LRF sensor, the rotation axis is extracted using a screw decomposition method.

Several calibration methods for a rotating 2D laser scanner system have been developed [20]. This study demonstrates that various constraints encountered in previously available methods can all be modeled as point-plane constraints. Furthermore, this paper proposes a method to minimize line-of-sight errors, which directly model the noise in the laser range finder measurements.

3.   Geometrical Model

3.1.   Notation

A scalar is denoted by the non-bold character x. The scalar components of a 3D point or vector are written as p_x, p_y, and p_z. Each of these represents the value of a given 3D point or vector in each corresponding axis.

Points are denoted using the lower case bold character **p**. Since there are several coordinate frames to consider, a given point can be represented by several notations, according to its reference coordinate frame. As an example, a point **p** in a coordinate frame with the origin located at c is denoted as ^{c}**p**. In several cases, the preceding superscript character that represents the reference coordinate frame may be omitted to save space and provide

more clarity. In this case, the reference coordinate frame is located at the global coordinate frame.

A vector is represented as a bold character with an arrow on top of it, e.g. $\overrightarrow{\mathbf{x}}$. Meanwhile to define a matrix, an uppercase bold character is used, e.g. $\mathbf{R}$. A coordinate system with the origin located at $\mathbf{c}$ is represented as $^{\mathbf{c}}\mathcal{F}$.

3.2.   Rotation System

An illustration of the 3D laser scanner is shown in Fig. 1. The 3D laser scanner system consists of a LRF sensor and a rotational base. In each rotation step, the sensor captures a single scanning line. Hence, by combining the scanning line from each rotation step, a 3D scene from a given environment is obtained.

A detailed illustration of the rotating LRF system is shown in Fig. 2. There are several parameters which should be determined in order to provide a reliable 3D scanning result.

The first parameter of the rotating LRF system is the rotation axis which defines the rotational path. A circular path is formed when a point is rotated along this axis. Fig. 2(a) shows the orientation of the rotation axis.

In this paper, the coordinate system axes of the LRF sensor are defined as follows. The z-axis points forward while the y-axis points upward. Thus, the scanning plane lies on the yz plane. As a result, the x-axis is perpendicular to the yz plane following the right-hand rule.

The second parameter of the rotating LRF system is the rotation radius. As shown in Fig. 2(b), the rotation radius can be represented as the length of the translation vector $\overrightarrow{\mathbf{t}}$. This vector is perpendicular to the rotation axis and its starting point lies on the rotation axis while its end point is located at the LRF origin at the initial rotation angle.
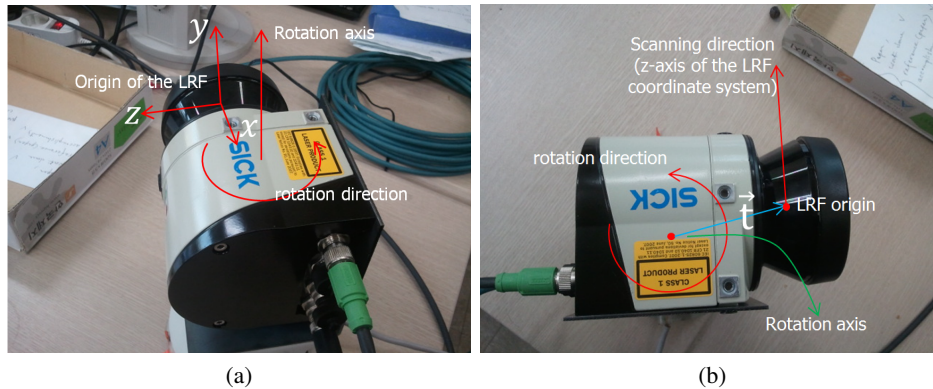

| (a) | (b) |

Fig. 2. Detailed illustration of the rotating system. The perspective view is shown in (a) while the top view is shown in (b). As shown in (a) and (b), the center of rotation and the LRF origin are not located at the same point. Furthermore, the rotation axis orientation is not parallel to the y-axis of the LRF coordinate frame as shown in (a). The translation vector is drawn as a blue arrow in (b).

3.3. Coordinate Frames

An illustration of the calibration system used for the rotating LRF system is shown in Fig. 3. The initial pose of the LRF sensor ($\mathbf{s}_0$) is used as the global coordinate frame and is denoted as $^{\mathbf{s}_0}\mathcal{F}$.

The pose of an LRF sensor changes at each rotation angles. At each rotation angle ϕ the LRF sensor moves to $\mathbf{s}_\phi$. Moreover, its coordinate frame is changed from the global coordinate frame point of view. However, the coordinate frame transformation between the initial position and the rotated position was not considered in this study. Using the calibration model presented in this paper, it is not necessary to know the coordinate frame transformation for each rotation step.

A point lying on the rotation axis, $\vec{\mathbf{u}}$, is defined as the rotation center. In the global coordinate frame, the rotation center is located at $\mathbf{c}$, which is $-\vec{\mathbf{t}}$ from the origin. At the rotation center, a coordinate frame, $^{\mathbf{c}}\mathcal{F}$, is defined. Despite using the body frame of the rotation system, a coordinate frame with an orientation equal to the global coordinate frame, $^{\mathbf{s}_0}\mathcal{F}$, is used.

A calibration pattern with an orientation $\vec{\mathbf{n}}$ is used in the calibration system. This calibration pattern is scanned by the LRF sensor. At each scanning angle θ the position of a point that lies on the calibration pattern, relative to the sensor pose, is known as $^{\mathbf{s}_\phi}\mathbf{p}_\theta$. Thus, for each rotation angle, ϕ, and scanning angle, θ, a point, $\mathbf{p}_{\phi,\theta}$, is obtained.

3.4. Virtual Points

In the coordinate frame $^{\mathbf{s}_\phi}\mathcal{F}$, the position of a scanned point, $\mathbf{p}_{\phi,\theta}$, is known. However, its position in the global coordinate frame remains unknown. In this section, the strategy used to define the position of a scanned point in the global coordinate system is explained.

To define the position of the scanned point, $\mathbf{p}_{\phi,\theta}$, in the global coordinate frame, a virtual point, $\mathbf{p}'_{\phi,\theta}$, is generated. A virtual point is defined as shown in (1). In each step of the rotation angle, ϕ, the position of the scanned point on the calibration pattern is known ($^{\mathbf{s}_\phi}\mathbf{p}_\theta$). This point corresponds to a virtual point in the LRF at the initial rotation angle. A
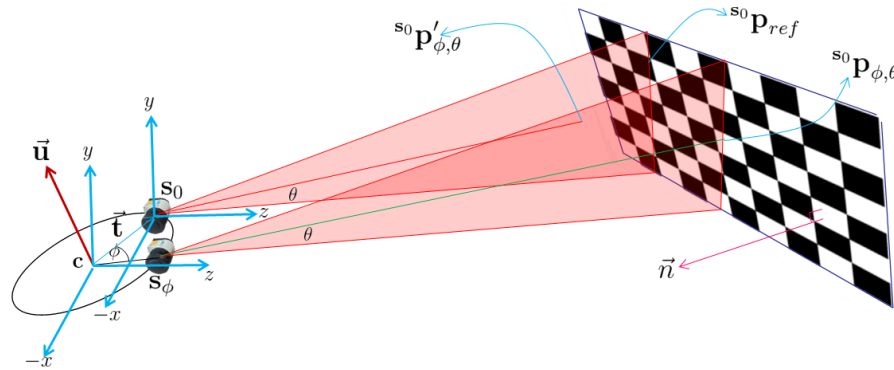

Fig. 3. Illustration of the calibration scheme. Note that the coordinate frame orientation in the center of rotation is equivalent to the coordinate frame of the LRF in the initial position.
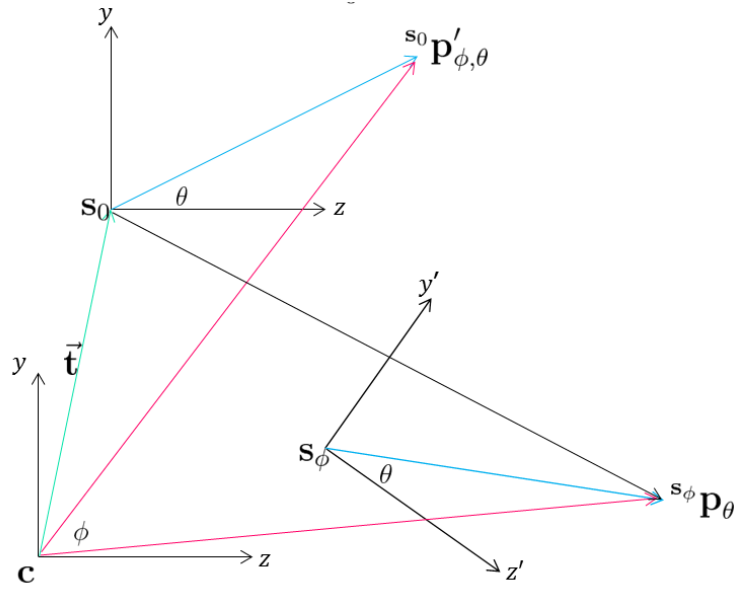
Fig. 4. Relationship between a virtual point and a real point shown in a simplified side view illustration. Note that in the local coordinate system, the virtual point and a real point are located at the same position. Moreover, the coordinate system used in the rotation center has the same orientation to the global coordinate system.

real point in the local coordinate frame, $^{s_\phi}\mathcal{F}$, is located at the same position with a virtual point in the global coordinate frame, $^{s_0}\mathcal{F}$. Alternatively, it can be stated that a virtual point satisfies (2). An illustration of this relation is shown in Fig. 4.

$$^{s_0}\mathbf{p}'_{\phi,\theta} = {}^{s_\phi}\mathbf{p}_\theta \tag{1}$$

$$\left\| {}^{s_0}\mathbf{s}_0 - {}^{s_0}\mathbf{p}'_{\phi,\theta} \right\| = \left\| {}^{s_0}\mathbf{s}_\phi - {}^{s_0}\mathbf{p}_\theta \right\| \tag{2}$$

The relationship between a real point and virtual point is shown in Fig. 3. To obtain a real point, $\mathbf{p}_{\phi,\theta}$, a virtual point, $\mathbf{p}'_{\phi,\theta}$, should be rotated based on the rotation system. A virtual point in the rotation system coordinate frame can be defined as shown in (3). This relationship is shown clearly in Fig. 4. Since the coordinate frame at the rotation center is equivalent to the global coordinate frame, $^{s_0}\mathcal{F}$, a virtual point, $\mathbf{p}'_{\phi,\theta}$, in the center of rotation coordinate frame, $^c\mathcal{F}$, is equal to the summation of the translation vector and its position in the LRF sensor coordinate frame at the initial pose.

$$^c\mathbf{p}'_{\phi,\theta} = \left({}^{s_0}\mathbf{p}'_{\phi,\theta} + {}^{s_0}\overrightarrow{\mathbf{t}} \right) \tag{3}$$

A real point in the center of rotation coordinate frame, $^c\mathbf{p}_{\phi,\theta}$, is obtained by rotating its corresponding virtual point. This relationship is defined in (4). By plugging (3) into (4), a new definition of the real point in the center of rotation coordinate frame is obtained, as shown in (5).
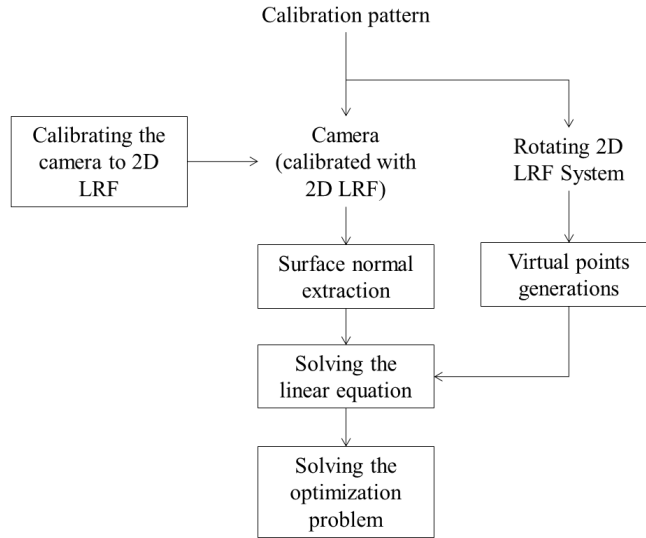
Fig. 5. Workflow of the proposed method.

$$^{\mathbf{c}}\mathbf{p}_{\phi,\theta} = \mathbf{R}_{\overrightarrow{\mathbf{u}},\phi}\,{}^{\mathbf{c}}\mathbf{p}_{\phi,\theta} \tag{4}$$

$$^{\mathbf{c}}\mathbf{p}_{\phi,\theta} = \mathbf{R}_{\overrightarrow{\mathbf{u}},\phi}\left({}^{\mathbf{s_0}}\mathbf{p}'_{\phi,\theta} + {}^{\mathbf{s_0}}\overrightarrow{\mathbf{t}}\right) \tag{5}$$

Since the global coordinate system is placed in the LRF at the initial pose, (5) must be converted into a position in the global coordinate system, resulting (6).

$$^{\mathbf{s_0}}\mathbf{p}_{\phi,\theta} = \mathbf{R}_{\mathbf{u},\phi}\left({}^{\mathbf{s_0}}\mathbf{p}'_{\phi,\theta} + {}^{\mathbf{s_0}}\mathbf{t}\right) - {}^{\mathbf{s_0}}\mathbf{t} \tag{6}$$

4.   Calibration Procedure

In this method, the surface normal of the calibration pattern is assumed to already be known, as determined by the camera-LRF calibration method. Several works concerning the camera-LRF calibration method are available [6, 10, 20, 24, 27]. The camera-LRF calibration method is not presented here since it is beyond the scope of this paper. The workflow of the proposed method is shown in Fig. 5.

4.1.   Linear Solution

In this work, the rotating LRF system was calibrated using a planar calibration pattern which was scanned using a rotating LRF sensor. This scanning result is a set of points which lies on the calibration pattern. Under ideal conditions, a point that lies on a plane means that it has zero distance to the calibration plane.

The distance from a point to a plane is computed using dot product operation between a vector and surface normal of the calibration plane. Thus, given a point, $\mathbf{p}_{\phi,\theta}$, that lies

on the calibration plane, its point-to-plane distance is always zero. This constraint can be formulated as shown in (7). The reference point, $\mathbf{p}_{ref}$, is a point that always lies on the calibration plane. A point scanned by the LRF sensor at the initial location is chosen as the reference point since it is free from the rotation distortion effect caused by the wrong selection of the rotation axis and translation vector.

By plugging (6) into (7), the new formula shown in (8) is obtained. Furthermore, this formula can be rearranged into (9). The rotation axis, $\overrightarrow{\mathbf{u}}$, and the translation vector, $\overrightarrow{\mathbf{t}}$, are the extracted from (9). To solve (9), its expanded matrix form is rearranged to form a linear equation.

The expanded form of (9) is shown in (10). It should be noted that the value of $p'_{\phi,\theta,x}$ is equal to zero for all values of ϕ and θ. The result of $\overrightarrow{\mathbf{n}}^{\top}\mathbf{p}_{ref}$ in (9) is denoted as w in (10). A compact form can be obtained through multiplication and rearrangement of (10), as shown in (11), which is a linear equation form. By having several data of virtual points from several calibration plane orientations, (11) is solvable.

$$\overrightarrow{\mathbf{n}}^{\top}\left(\mathbf{p}_{\phi,\theta}-\mathbf{p}_{ref}\right)=0 \tag{7}$$

$$\overrightarrow{\mathbf{n}}^{\top}\left(\mathbf{R}_{\overrightarrow{\mathbf{u}},\phi}\left(\mathbf{p}'_{\phi,\theta}+\overrightarrow{\mathbf{t}}\right)-\overrightarrow{\mathbf{t}}-\mathbf{p}_{ref}\right)=0 \tag{8}$$

$$\mathbf{n}^{\top}\mathbf{R}_{\overrightarrow{\mathbf{u}},\phi}\left(\mathbf{p}'_{\phi,\theta}+\overrightarrow{\mathbf{t}}\right)-\overrightarrow{\mathbf{n}}^{\top}\mathbf{t}=\overrightarrow{\mathbf{n}}^{\top}\mathbf{p}_{ref} \tag{9}$$

$$\begin{bmatrix}n_x\\n_y\\n_z\end{bmatrix}^{\top}\begin{bmatrix}a\ b\ c\\d\ e\ f\\g\ h\ i\end{bmatrix}\begin{bmatrix}1\ 0\ 0\ &0\\0\ 1\ 0\ &p'_{\phi,\theta,y}\\0\ 0\ 1\ &p'_{\phi,\theta,z}\end{bmatrix}\begin{bmatrix}t_x\\t_y\\t_z\\1\end{bmatrix}-\begin{bmatrix}n_x\\n_y\\n_z\end{bmatrix}^{\top}\begin{bmatrix}t_x\\t_y\\t_z\end{bmatrix}=w \tag{10}$$

Equation (11) is solvable using a linear equation system solver such as Gaussian elimination. Furthermore the solution of (11) is sufficient to generate a translation vector and rotation axis. However, a lot of calibration pattern poses are required to provide enough data to solve the linear equation. Hence, a further rearrangement is needed.

A rotation matrix representing rotation along an arbitrary axis, $\overrightarrow{\mathbf{u}}$, is defined in (12). A detailed explanation of this rotation matrix has been previously provided [22]. By representing the rotation matrix as (12), the linear equation (11) can be rearranged to (13) and (14). This new form is solvable by using only two poses of the calibration pattern. As shown in Table 1, this method requires the least number of pairs of the LRF-scan and camera image compared to the other calibration methods.

$$\begin{bmatrix}p'_{\phi,\theta,y}n_x\\p'_{\phi,\theta,z}n_x\\p'_{\phi,\theta,y}n_y\\p'_{\phi,\theta,z}n_y\\p'_{\phi,\theta,y}n_z\\p'_{\phi,\theta,z}n_z\\n_x\\n_y\\n_z\end{bmatrix}^{\top}\begin{bmatrix}b\\c\\e\\f\\h\\i\\at_x+bt_y+ct_z-t_x\\dt_x+et_y+ft_z-t_y\\gt_x+ht_y+it_z-t_z\end{bmatrix}=w \tag{11}$$

$$R_{u,\phi} = \begin{bmatrix} cos\phi + u_x^2\left(1 - cos\phi\right) & u_xu_y\left(1 - cos\phi\right) - u_z sin\phi & u_xu_z\left(1 - cos\phi\right) + u_y sin\phi \\ u_yu_x\left(1 - cos\phi\right) + u_z sin\phi & cos\phi + u_y^2\left(1 - cos\phi\right) & u_yu_z\left(1 - cos\phi\right) - u_x sin\phi \\ u_zu_x\left(1 - cos\phi\right) - u_y sin\phi & u_zu_y\left(1 - cos\phi\right) + u_x sin\phi & cos\phi + u_z^2\left(1 - cos\phi\right) \end{bmatrix}$$

$$(12)$$

$$\begin{bmatrix} p'_{\phi,\theta,x}n_x\left(1 - cos\phi\right) \\ -p'_{\phi,\theta,x}n_x sin\phi \\ p'_{\phi,\theta,y}n_y\left(1 - cos\phi\right) \\ p'_{\phi,\theta,y}n_z\left(1 - cos\phi\right) \\ p'_{\phi,\theta,y}n_z sin\phi \\ p'_{\phi,\theta,z}n_x\left(1 - cos\phi\right) \\ p'_{\phi,\theta,z}n_x sin\phi \\ p'_{\phi,\theta,z}n_y\left(1 - cos\phi\right) \\ -p'_{\phi,\theta,z}n_y sin\phi \\ p'_{\phi,\theta,z}n_z\left(1 - cos\phi\right) \\ n_x cos\phi \\ n_x sin\phi \\ n_x \\ n_y cos\phi \\ n_y sin\phi \\ n_y \\ n_z cos\phi \\ n_z sin\phi \\ n_z \end{bmatrix}^\top \begin{bmatrix} u_xu_y \\ u_z \\ u_y^2 \\ u_yu_z \\ u_x \\ u_xu_z \\ u_y \\ u_yu_z \\ u_x \\ u_z^2 \\ t_x - \left(t_xu_x^2 + t_yu_xu_y + t_zu_xu_z\right) \\ -t_yu_z + t_zu_y \\ \left(t_xu_x^2 + t_yu_xu_y + t_zu_xu_z\right) - t_x \\ t_y - \left(u_xu_yt_x + u_y^2t_y + u_yu_zt_z\right) \\ u_zt_x - u_xt_z \\ \left(u_xu_yt_x + u_y^2t_y + u_yu_zt_z\right) - t_y \\ t_z - \left(u_zu_xt_x + u_zu_yt_y + u_z^2t_z\right) \\ -u_yt_x + u_xt_y \\ \left(u_zu_xt_x + u_zu_yt_y + u_z^2t_z\right) - t_z \end{bmatrix} = w_2 \qquad (13)$$

$$w_2 = \overrightarrow{\mathbf{n}}^\top \mathbf{p}_{ref} - \left(p'_{\phi,\theta,y}n_y + p'_{\phi,\theta,z}n_z\right)cos\phi \qquad (14)$$

All components of the rotation axis are extracted directly from the solution of (13). Having all components of the rotation axis, the translation vector is extracted from the solution of (13).

Table 1. Minimum LRF-scan and image pairs. The numbers in the brackets represent the number of pairs required to obtain a unique solution. The calibration method proposed in this paper requires the smallest amount of LRF-scan and image pairs compared to the other methods.

Method	Correspondences	Scan-Image Pairs	
		Original	Point-Plane [19]
Zhang [27]	line-on-plane	5	3 (4)
Wasielewski [25]	point-on-image-line	9	6 (7)
Li [14]	point-on-image-line	5	3 (4)
Our	point-on-a-plane	2 (3)	-

4.2. Optimization

The linear solution in section 4.1 was obtained by minimizing the algebraic error. To obtain the optimal calibration parameters, an optimization method is performed by minimizing the geometrical error in the calibration system.

$$\epsilon = \overrightarrow{\mathbf{n}}^{\top} \left(\mathbf{R}_{\overrightarrow{\mathbf{u}},\phi} \left(\mathbf{p}'_{\phi,\theta} + \overrightarrow{\mathbf{t}} \right) - \overrightarrow{\mathbf{t}} - \mathbf{p}_{ref} \right) \tag{15}$$

$$\underset{\overrightarrow{\mathbf{u}},\overrightarrow{\mathbf{t}}}{\operatorname{argmin}} \sum_{j=1}^{M} \sum_{i=1}^{N} \left(\overrightarrow{\mathbf{n}}^{\top} \left(\mathbf{R}_{\overrightarrow{\mathbf{u}},\phi_j} \left(\mathbf{p}'_{\phi,\theta_i} + \overrightarrow{\mathbf{t}} \right) - \overrightarrow{\mathbf{t}} - \mathbf{p}_{ref} \right) \right)^2 + \gamma \overrightarrow{\mathbf{u}}^{\top} \overrightarrow{\mathbf{t}} \tag{16}$$

The geometrical error is defined as the point-to-plane distance error (15), which is the combination of all point-to-plane distance errors from the calibration data. The wrongly chosen calibration parameters affect the value of this point-to-plane distance error. Since the rotation axis and the translation vector should be perpendicular, a penalty score is added in the case where these two parameters are not perpendicular to each other. Thus, the optimization problem is defined as shown in (16). The γ value is a large constant that affects the penalty value in the case where the rotation axis and the translation vector are not perpendicular.

The optimization problem defined in (16) was solved using a non-linear optimization method. The Levenberg-Marquardt optimization method, [13, 16, 15], has been used to solve the minimization problem.

5. Simulations

The proposed method was tested on a simulation system developed using MATLAB. The rotation axis was chosen randomly, deviated under 45 degrees from $\mathbf{y}$, which is the y-axis of the sensor coordinate frame at the initial position. The translation vector is chosen as a vector perpendicular to both $\overrightarrow{\mathbf{u}}$ and $\mathbf{y}$. The translation vector is defined in (17), where r is the distance between the center of rotation and the sensor at the initial position. Points are generated as the ground truth data based on the calibration plane parameters. From each point, laser range data is generated. Noise is added to the laser range data to mimic the original system. The LRF measurement noise is set from 12 mm to 30 mm, which are the statistical error and systematic error of SICK LMS 111, respectively.
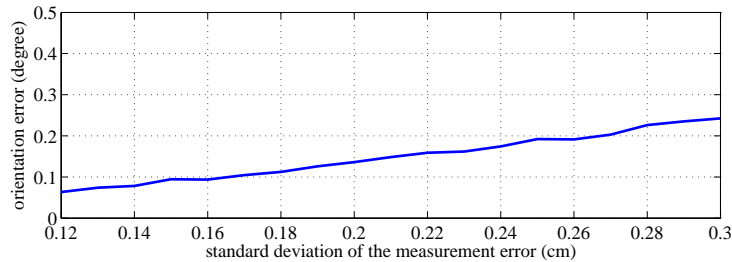

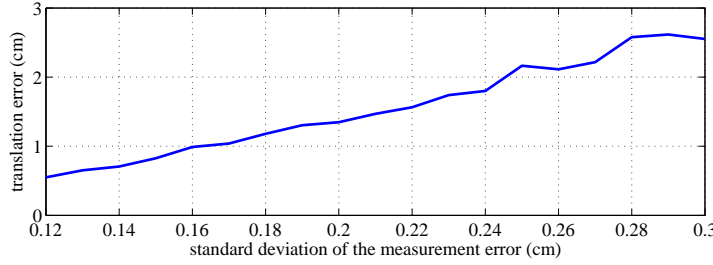**Fig. 6.** Relationship between the noise and orientation error.

Fig. 7. Relationship between the noise and translation error.

Table 2. Relationship between the number of calibration pattern poses and the resulting error. The error resulting from calibration with 9 poses of the calibration pattern is relatively small

error	number of calibration poses							
	2	3	4	5	6	7	8	9
orientation	70.11	37.14	1.53	0.27	0.14	0.10	0.08	0.06
position	1804.16	419.83	8.90	1.72	1.11	0.84	0.68	0.55

$$\overrightarrow{\mathbf{t}} = \left(\overrightarrow{\mathbf{u}} \times \mathbf{y} \right) r \tag{17}$$

Laser range data for each rotation angle, ϕ, and scanning angle, θ, is defined in (18). Based on the laser data, virtual points are defined in (19). Using the virtual points and calibration plane parameters data, the calibration process was simulated.

$$l_{\phi,\theta} = \frac{\overrightarrow{\mathbf{n}}^{\top} \left(\mathbf{p}_{ref} - \mathbf{R}_{\overrightarrow{b},\phi} \overrightarrow{\mathbf{t}} + \overrightarrow{\mathbf{t}} \right)}{cos\theta} \tag{18}$$

$$\mathbf{p}'_{\phi,\theta} = \frac{\mathbf{R}_{y,\theta}\mathbf{z}}{\|\mathbf{R}_{y,\theta}\mathbf{z}\|} \left(l_{\phi,\theta} + \varepsilon \right) \tag{19}$$

The first goal of the simulation was to determine the relationship between the number of calibration pattern poses and the resulting calibration error. In this case, 8 schemes are considered. The number of calibration pattern poses varies from 2 to 9 for each scheme. In each schemes, the position error and orientation error are averaged from 100 calibration trials, where in each trial, the calibration pattern poses are generated randomly. The result of these simulation schemes is shown in Table 2.The proposed method is able to extract the rotation system parameter with a reasonable precision. More results are shown in Fig. 12 and Fig. 13. Using 30 poses of the calibration pattern, the resulting orientation and translation errors are 0.018 degree and 0.2 cm, respectively.

The second goal of the simulation was to determine the relationship between the measurement error given by the LRF sensor and the resulting calibration error. In this case, the standard deviation of the measurement error (σ) given by the LRF sensor was emulated to mimic the measurement error of the SICK LMS 111 sensor. The position error
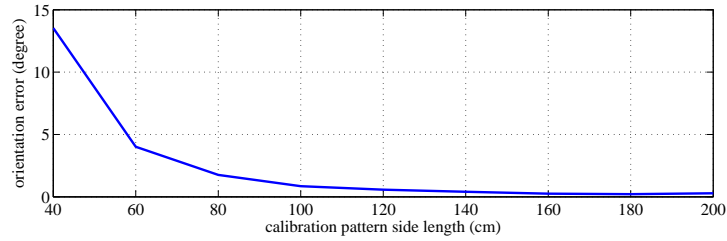
Fig. 8. Relationship between the size of the calibration pattern and the orientation error.
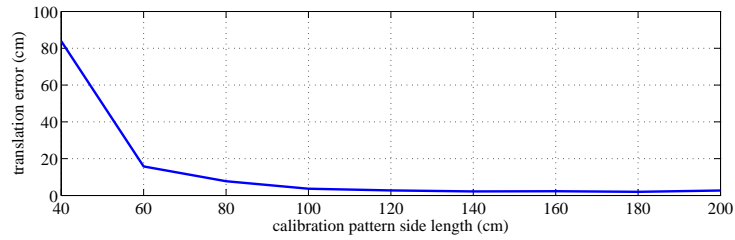

Fig. 9. Relationship between the size of the calibration pattern and the translation error.
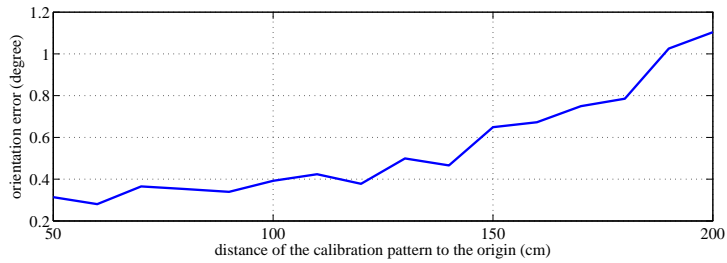

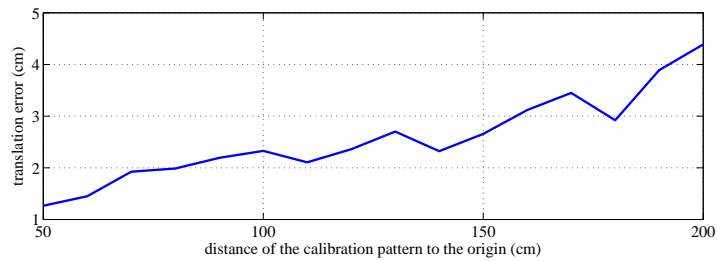**Fig. 10.** Relationship between the distance of the calibration pattern and the orientation error.

Fig. 11. Relationship between the distance of the calibration pattern and the translation error.

Table 3. Optimization result of the translation vector.

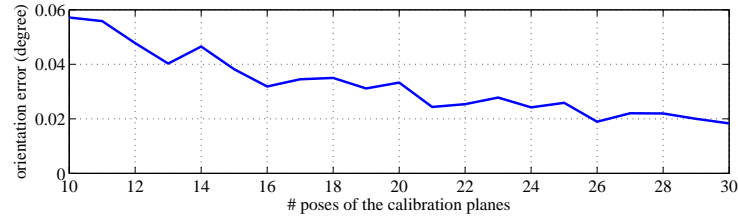|	initial			final		
	tx	ty	tz	tx	ty	tz
translation vector (cm)	-1.807	0.000	-4.638	-1.802	-0.016	-4.640
translation error (cm)	0.052			0.049		

Fig. 12. Relationship between the number of the calibration pattern poses and the orientation error.
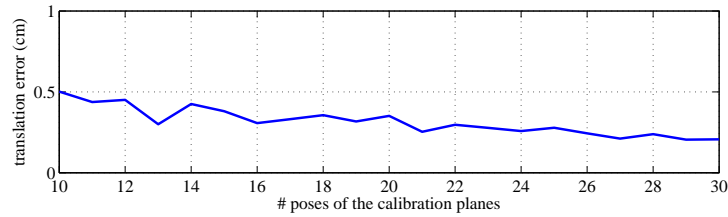

Fig. 13. Relationship between the number of the calibration pattern poses and the translation error.

and orientation error were extracted similarly to the previous simulation case, which are the average values obtained from 100 trials for each value of σ.

The relationship between the value of σ and the orientation error is shown in Fig. 6. Meanwhile, the relationship between the value of σ and the translation error is shown in Fig. 7. The number of calibration pattern poses was set to be 9. As expected, the orientation error increased as the value of σ increased. However, as shown in the graph, the orientation error obtained at the maximum value of σ of around 0.25 degrees is still reasonable.

The third goal of the simulation was to determine the relationship between the size of the calibration pattern and the resulting calibration error. As shown in Fig. 8, the calibration error decreases as the calibration pattern size increases. It is sufficient to use the calibration pattern with a side length of 150 cm to obtain the rotation axis with an error below 1 degree. The calibration pattern size affects the translation error, as shown in Fig. 9. As expected, the larger the calibration pattern, the lower the error. More data are available when a larger sized calibration pattern is used.

The fourth goal of the simulation was to determine the relationship between the effect of the calibration pattern distance to the calibration result. For this case, a fixed calibration pattern size was used. The calibration pattern size was set with a length of 100 cm. As expected, the longer the calibration pattern, the less accurate the calibration result, as shown

in Fig. 10 and Fig. 11. At far distances, the number of points lying on the calibration pattern decreases.

The fifth goal of the simulation was to observe the effect of the proposed optimization method on the calibration result. In the simulation, the parameter γ was set at 100. In this case, the optimization method was only used to refine the translation vector. The rotation vector was not refined in the optimization process since it already has a small error and is quite precise. From the simulation results, it is seen in Table 3 that the optimization process did not provides a significant improvement to the translation error.

6.   Conclusion

A novel calibration method for a rotating LRF system was proposed. The method relies on the solution of linear equations constructed by applying point-plane constraints of the scanned calibration pattern. This method is solvable using 2 poses of the calibration pattern, which offers simplicity compared to other methods. Several simulation schemes were performed to examine the effect of the sensor noise, calibration pattern size, position of the calibration pattern, and number of calibration patterns on the calibration results. In future work, improvement of the calibration results and implementation to real systems will be considered.

References

1. Abaei, G., Selamat, A.: A survey on software fault detection based on different prediction approaches. Vietnam Journal of Computer Science 1(2), 79–95 (2014), http://dx.doi.org/10.1007/s40595-013-0008-z
2. Cortes, C., Vapnik, V.: Support-vector networks. Machine. Learn. 20(3), 273–297 (Sep 1995)
3. Do, T.N.: Parallel multiclass stochastic gradient descent algorithms for classifying million images with very-high-dimensional signatures into thousands classes. Vietnam Journal of Computer Science 1(2), 107–115 (Jan 2014)
4. Fan, H., Li, G., Dong, L.: The calibration algorithm between 3d laser range finder and platform. In: International Joint Conference on Computational Sciences an Optimization (CSO). pp. 781–783 (2009)
5. Heide, F., Xiao, L., Heidrich, W., Hullin, M.B.: Diffuse mirrors: 3D reconstruction from diffuse indirect illumination using inexpensive time-of-flight sensors. In: IEEE Conference on Computer Vision and Pattern Recognition (CVPR). p. to appear (Jun 2014)
6. Hoang, V.D., Hernández, D.C., Jo, K.H.: Simple and efficient method for calibration of a camera and 2d laser rangefinder. In: Intelligent Information and Database Systems. pp. 561–570 (2014)
7. Hoang, V.D., Hernández, D.C., Le, M.H., Jo, K.H.: 3d motion estimation based on pitch and azimuth from respective camera and laser rangefinder sensing. In: IEEE international conference on intelligent robots and systems. pp. 735–740 (2013)
8. Hoang, V.D., Jo, K.H.: Path planning for autonomous vehicle based on heuristic searching using online images. Vietnam Journal of Computer Science pp. 1–12 (2014), http://dx.doi.org/10.1007/s40595-014-0035-4

9. Jakóbczak, D.: Curve interpolation and shape modeling via probabilistic nodes combination. Vietnam Journal of Computer Science 1(3), 141–153 (2014), http://dx.doi.org/10.1007/s40595-014-0016-7

10. Jung, J.J.: Contextual Synchronization for Efficient Social Collaborations in Enterprise Computing: a Case Study on TweetPulse. Concurrent Engineering-Research and Applications 21(3), 209–216 (2013).

11. Kurnianggoro, L., Hoang, V.D., Jo, K.H.: Calibration of rotating 2d laser range finder using circular path on plane constraints. In: New Trends in Computational Collective Intelligence. pp. 155–163. Springer (2015), http://dx.doi.org/10.1007/978-3-319-10774-5_15

12. Le, B., Nguyen, H., Tran, D.: A robust fingerprint watermark-based authentication scheme in h.264/avc video. Vietnam Journal of Computer Science 1(3), 193–206 (2014), http://dx.doi.org/10.1007/s40595-014-0021-x

13. Levenberg, K.: A method for the solution of certain problems in least squares. Quarterly Applied Math 2, 164–168 (1944)

14. Li, G., Liu, Y., Dong, L., Cai, X., Zhou, D.: An algorithm for extrinsic parameters calibration of a camera and a laser range finder using line features. In: IEEE/RSJ International Conference on Intelligent Robots and Systems. pp. 3854–3859 (2007)

15. Marquardt, D.: An algorithm for least squares estimation of nonlinear parameters. SIAM Journal of Applied Math 11, 431–441 (1963)

16. Mor, J.J.: The levenberg-marquardt algorithm: Implementation and theory. In: Watson, G.A. (ed.) Lecture Notes in Mathematics, vol. 630, pp. 105–116. Springer-Verlag (1977)

17. Pham, X.H., Jung, J.J.: Recommendation System Based on Multilingual Entity Matching on Linked Open Data. Journal of Intelligent & Fuzzy Systems 27(2) 589–599 (2014)

18. Roh, C.H., Lee, W.B.: Development of a 3d tangible-serious game for attention improvement. International Journal of Intelligent Information and Database Systems 8(2), 85–96 (Jul 2014)

19. So, E., Basso, F., Menegatti, E.: Calibration of a rotating 2D laser range finder using point-plane constraints. Journal of Automation, Mobile Robotics & Intelligent Systems 7(2), 30–38 (2013)

20. So, E., Menegatti, E.: A unified approach to extrinsic calibration between a camera and a laser range finder using point-plane constraints. In: Proceedings of the 1st International Workshop on Perception for Mobile Robots Autonomy (2012)

21. Song, S., Xiao, J.: Sliding shapes for 3d object detection in depth images. In: Computer Vision - ECCV 2014 - 13th European Conference, Zurich, Switzerland, September 6-12, 2014, Proceedings, Part VI. pp. 634–651 (2014)

22. Taylor, C.J., Kriegman, D.J.: Minimization on the lie group so(3) and related manifolds. Tech. Rep. 9405, Yale University (1994)

23. Uckermann, A., Haschke, R., Ritter, H.: Realtime 3d segmentation for human-robot interaction. In: IEEE international conference on intelligent robots and systems. pp. 2136–2143 (2013)

24. Vasconcelos, F., Barreto, J.P., Nunes, U.: A minimal solution for the extrinsic calibration of a camera and a laser-rangefinder. IEEE Trans. Pattern Anal. Mach. Intell. (PAMI) pp. 2097–2107 (2012)

25. Wasielewski, S., Strauss, O.: Calibration of a multi-sensor system laser rangefinder/camera. In: Intelligent Vehicles Symposium. pp. 472–477 (1995)

26. Yang, G., Zhengchun, D., Zhenqiang, Y.: Calibration method of three dimensional (3d) laser measurement system based on projective transformation. In: International Conference on Measuring Technology and Mechatronics Automation (ICMTMA). pp. 666–671 (2011)

27. Zhang, Q., Pless, R.: Extrinsic calibration of a camera and laser range finder (improves camera calibration). In: International Conference on Intelligent Robots and Systems (IROS). pp. 2301–2306 (2004)

Laksono Kurnianggoro received his bachelor of engineering from Universitas Gadjah Mada, Indonesia, in 2010. He is currently a Ph.D. student at the Graduate School of Electrical Engineering, University of Ulsan, Ulsan, Korea. He is actively participating as a member of societies such as IEEE. His research interest include stereo vision, 3D image processing, computer vision, and machine learning.

Van-Dung Hoang received his bachelor of informatics from Hue University, Vietnam, in 2002, and master of computer sciences from Hanoi National University of Education, Vietnam, in 2007. Since 2002, he has been serving as a lecturer in University of Quangbinh, Vietnam. He is currently a Ph.D. candidate at the Graduate School of Electrical and Computer Engineering, University of Ulsan, Ulsan, Korea. He is actively participating as a member of the societies as IEEE, ICROS. His research interests include pattern recognition, machine learning, computervision, and vision based robotics.

Kang-Hyun Jo received his Ph.D.degree from Osaka University, Japan, in 1997. He then joined the School of Electrical Eng., University of Ulsan, right after having one years experience at ETRI as a postdoc research fellow. Dr.Jo has been actively serving the societies for many years as a director of ICROS (Institute of Control, Robotics and Systems)and SICE (Society of Instrumentation and Control Engineers, Japan) as well as IEEE IES TC-HF Chair. He is currently contributing as an editorial member for a few renowned international journals, such as IJCAS (International Journal of Control, Automation and Systems), TCCI (Transactions on Computational Collective Intelligence, Springer) and IteN (IES Technical News, online publication of IEEE). He has been involved in organizing many international conferences such as ICCAS, FCV, IFOST, ICIC and IECON. He has visited Kyushu University, KIST and University of California Riverside for performing his research activity. His research interest covers a wide area that focuses on computer vision,robotics, and ambient intelligence.